

Effect of ocean gateways on the global ocean circulation in the late Oligocene and early Miocene

Anna von der Heydt¹ and Henk A. Dijkstra^{2,3}

Received 18 February 2005; revised 10 October 2005; accepted 2 November 2005; published 14 March 2006.

[1] We investigate the effect of changes in the tectonic boundary conditions on global ocean circulation patterns. Using a fully coupled climate model in an idealized setup, we compare situations corresponding to the late Oligocene, the early Miocene, and present day. The model results show the existence of a flow reversal through the Panama Seaway between the Oligocene and Miocene. This flow reversal is induced by global tectonic changes related to the widening of the Southern Ocean passages and the closing of the Tethys Seaway. It mainly involves the wind-driven ocean circulation, in agreement with previous model studies. The global thermohaline circulation in the Oligocene and Miocene simulations is significantly different from the present-day conveyor circulation, as there is deepwater formation in both the North Atlantic and the North Pacific oceans. In particular, in the Oligocene simulation the salinity contrast between the Atlantic and Pacific oceans is reduced because of water mass exchange through the low-latitude connections between the two oceans.

Citation: von der Heydt, A., and H. A. Dijkstra (2006), Effect of ocean gateways on the global ocean circulation in the late Oligocene and early Miocene, *Paleoceanography*, 21, PA1011, doi:10.1029/2005PA001149.

1. Introduction

[2] Climate proxies indicate that significant climatic and oceanographic changes have occurred across the Oligocene/Miocene boundary [Miller *et al.*, 1991; Wright *et al.*, 1992; Paul *et al.*, 2000; Zachos *et al.*, 2001]. After the late Oligocene warming period when the long-term glaciation of Antarctica terminated, climate remained relatively warm for the rest of the Oligocene (27–24 Ma). In the early Miocene (23–17 Ma), after the Oligocene/Miocene boundary, the $\delta^{18}\text{O}$ values are higher, indicating slightly colder climatic conditions. In the early Miocene, many warm water corals in the Caribbean Sea disappeared [Edinger and Risk, 1994, 1995]. Changes in continental configuration may have been responsible for the climatic change from the late Oligocene to the early Miocene. However, changes in atmospheric composition may also have played a role.

[3] Important tectonic changes took place in the late Oligocene and early Miocene, which must have been associated with large-scale changes in the global ocean circulation. In the Eocene and early Oligocene, the Tasmanian gateway opened in the Southern Ocean by northward movement of Australia [Ocean Drilling Program, 2001]. Also, South America moved northward in the early Oligocene, thereby opening Drake Passage [Barker and Burrell, 1977; Kennett, 1977; Lawver, 1992]. With the opening of these gateways, the Antarctic Circumpolar Current strength-

ened in the Oligocene. Another important tectonic event occurred in the equatorial region. In the Cretaceous and early Tertiary, the continents were positioned such that a circumequatorial ocean current was possible; the Tethys current transported water westward from the Indian Ocean through the Tethys Seaway into the Atlantic Ocean [Hallam, 1969]. From the Atlantic, water was transported through the Panama Seaway back into the Pacific Ocean. In the early Miocene, the Tethys Seaway shallowed and closed as the African and Eurasian plates collided [Dercourt *et al.*, 2000]. This rendered a circumequatorial current impossible [Ricou, 1987].

[4] Within a 1.5-layer shallow-water model of the wind-driven ocean circulation [Omta and Dijkstra, 2003] found that the transport through the Panama Seaway reversed from westward in the late Oligocene to eastward in the Miocene. They showed that the transport through the Panama Seaway directly depended on the transports through the Drake Passage and the Tethys Seaway. In this way, the narrowing of the Tethys Seaway in the early Miocene and the widening of the Drake Passage caused the flow reversal through the Panama Seaway. It was argued by von der Heydt and Dijkstra [2005] that this flow reversal lead to a significant cooling of the Caribbean surface waters and hence may have been the reason for the demise of warm water corals in the early Miocene.

[5] By analyzing the same fully coupled climate model simulations as given by von der Heydt and Dijkstra [2005] plus similar simulations for the present-day continental geometry, our aim here is to study the effect of gateways on the patterns of the global ocean circulation. More specifically, we will address the following questions: (1) Is the suggested physical mechanism for this flow reversal given by Omta and Dijkstra [2003] the same as in the fully coupled climate model? (2) What impact does the Atlantic-Pacific flow reversal have on the thermohaline circulation in

¹Institute for Marine and Atmospheric Research, Department of Physics and Astronomy, Utrecht University, Utrecht, Netherlands.

²Department of Atmospheric Science, Colorado State University, Fort Collins, Colorado, USA.

³Also at Institute for Marine and Atmospheric Research, Department of Physics and Astronomy, Utrecht University, Utrecht, Netherlands.

the Atlantic and Pacific? (3) How is the global ocean circulation affected by the tectonic changes that have occurred across the Oligocene/Miocene boundary?

[6] The paper is organized as follows. In section 2, the climate model and the initial and boundary conditions are described and the equilibration of the model solution is discussed. As we use an idealized setup, results of two control simulations with present-day continental configuration are presented to identify deficiencies and biases in the model results. Results from the Oligocene and Miocene simulations are presented in section 3. In section 4.1, we analyze the Atlantic-Pacific flow reversal and compare the results with those of *Omta and Dijkstra* [2003]. The effect of the tectonic changes on the thermohaline circulation and its implications for the global climate are discussed in section 4.2. In section 5, we summarize the results.

2. Model Description

[7] We use the Community Climate System Model (CCSM) version 1.4 developed at the National Center for Atmospheric Research (NCAR). This is a model in which the atmosphere, ocean, sea ice and land surface components are fully coupled with detailed parameterizations of physical processes in each component. Version 1 of this model is described by *Boville and Gent* [1998]. The atmospheric model is the Community Climate Model (CCM) version 3.6, a spectral general circulation model with 18 levels in the vertical [*Kiehl et al.*, 1998]. Here it is run at T31 resolution which results in a resolution of about 3.6° in latitude and 3.75° in longitude. It is coupled to the Land Surface Model (LSM 1.2), a one-dimensional model of energy, momentum, water and CO_2 exchange between the atmosphere and the land surface. LSM provides a comprehensive treatment of land surface processes and has specified vegetation types [*Bonan*, 1998]. The ocean model is the NCAR CSM Ocean Model (NCOM 1.5), a general circulation model on a stretched grid with 0.9° meridional grid spacing at the equator, 1.8° at high latitudes, 3.6° zonal grid spacing, and 25 vertical levels. It uses the Gent-McWilliams eddy mixing parameterization and a nonlocal k profile boundary layer parameterization. The sea ice model (CSIM 2.2.9) includes thermodynamic ice processes and ice dynamics based on the cavitating fluid solution [*Weatherly et al.*, 1998]. It is run at the same resolution as the ocean model.

2.1. Forcing and Boundary Conditions

[8] We performed two simulations with two different continental boundaries, one representing the late Oligocene and the other representing the early Miocene. The only differences are the continental geometry and the slightly different vegetation types (see below). The continental geometries are based on the plate tectonic reconstructions available at ODSN (<http://www.odsn.de>) and are the same as used by *Omta and Dijkstra* [2003] and *von der Heydt and Dijkstra* [2005]. They are idealized as they are interpolated to the relatively coarse model resolution, but contain the main tectonic changes between the late Oligocene and early Miocene. The Tethys Seaway is open in the late Oligocene

and closed in the early Miocene. The Tasmanian gateway widens from the Oligocene to the Miocene because of the northward movement of Australia. The Panama Seaway is open in both simulations. There is a small gap between India and Asia in the Oligocene geometry. This is probably not realistic for the late Oligocene, when this seaway was already closed or very shallow. However, the gap is narrow enough such that the flow through it remains negligibly small.

[9] In order to purely study the effect of the opening or closing of ocean gateways we use an ocean model with a flat bottom of 5000 m depth. The land is also kept flat with a constant elevation of 350 m. For the land surface model we use idealized, “best guess” land surface conditions and vegetation; that is, we impose constant mean soil color and texture, and zonally constant vegetation distributions on the basis of the climate history maps given by C. R. Scotese (PALEOMAP Web site, available at <http://www.scotese.com>, 2002). These distributions differ only slightly between the Oligocene and Miocene; the most important difference is that, in the Oligocene, there is a smaller part of Antarctica covered with ice. The atmospheric CO_2 level has been estimated to be smaller than about 2 to 2.5 times the present-day value during both periods [*Crowley and North*, 1991; *Royer et al.*, 2001]. As we aim to investigate the effect of the continental geometry on the global ocean circulation, we keep the CO_2 concentration constant ($p\text{CO}_2 = 710$ ppm) and equal in both simulations. The solar constant is set to the present-day value.

2.2. Spin-up of the Model

[10] To reach a climatic equilibrium, we follow the procedure as described by *Huber and Sloan* [2001]. We briefly summarize the method here:

[11] 1. The fully coupled CCSM is integrated for 20 years. Initial condition for the ocean is a cosine shaped sea surface temperature (SST) profile varying from 28°C at the equator to 3°C at the poles, and a vertical temperature field linearly interpolated between the SST and 1°C deep-sea temperature. The salinity is taken constant, and the velocities are zero. The atmosphere is initialized with a zonally constant temperature field with temperatures varying from 28°C at the equator and 3°C at the poles and the zonal velocity determined from the thermal wind balance. Sea ice concentration is set to zero at the beginning.

[12] 2. The ocean and sea ice models are driven by the last 5 years of output of the atmosphere and land model from the previous step. The deep ocean is accelerated, as noted by *Danabasoglu et al.* [1996], by $50\times$ tracer time steps. This configuration is integrated for 20 years, i.e., for 1000 deep-ocean years.

[13] 3. The fully coupled model is integrated for 20 years. The ocean and ice components are initialized with the conditions from the end of the previous step, whereas the atmosphere and land models start from the last state of the penultimate step.

[14] The last two steps are repeated twice. The last fully coupled run is integrated for 200 years. In total the model is integrated for 320 years, corresponding to 3260 deep-ocean years. For the Miocene simulation, an additional iteration (repeat of steps 2 and 3) after year 320 was necessary to

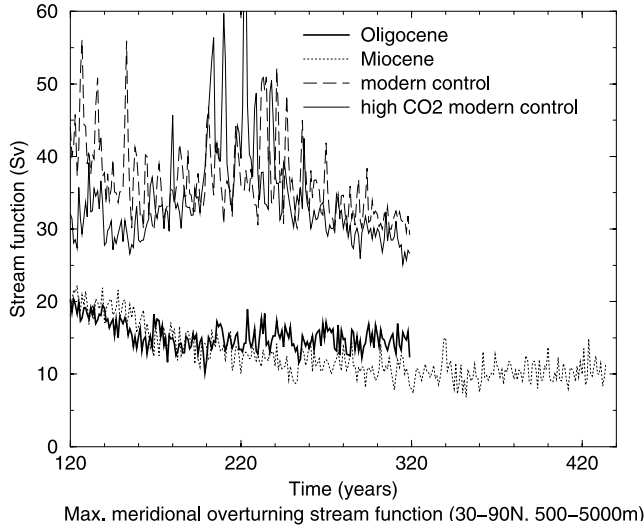


Figure 1. Time series of the maximum value of the global meridional overturning stream function in the Northern Hemisphere (in the area 30°–90°N) for the late Oligocene (bold solid line), the early Miocene (dotted line), the modern control (dashed line), and the high CO₂ modern control (thin solid line) simulations.

ensure convergence toward a stable climate state, with the last fully coupled run integrated for 95 years. We use the time average of the last 25 years of model output from the fully coupled run for analysis in this study (years 295–320 for the Oligocene and present-day simulations and years 410–435 for the Miocene simulation).

[15] The model has reached a quasi-equilibrium state at the end of this procedure. As the ocean is the slowest component in the model, we show in Figure 1 a time series of the maximum value of the global meridional overturning stream function in the Northern Hemisphere over the last fully coupled run. It shows variability on many timescales for all simulations. There is a small drift visible in Figure 1. During the first 50 years, the Oligocene overturning stream function decreases more than during the next 150 years, indicating that it is converging toward an equilibrium state. In the Miocene simulation, the overturning stream function converges toward an equilibrium state only after an additional iteration of the spin up procedure. In both modern day geometry simulations the overturning strength is decreasing over the first 50 years; however, during the last 150 years it seems to first increase and then decrease again, which makes it difficult to speak of an unidirectional drift. In

addition, for the modern day geometry control simulation with preindustrial CO₂ level, the drift in the volume-averaged ocean temperature over this period is already very small; see Table 1. Therefore we assume that the thermohaline circulation has already reached an equilibrium state and shows natural variability on timescales as long as 50–100 years. The same seems to hold for the modern day geometry control simulation with high CO₂ level; however, there the temperature drift is similar to the Miocene simulation. The linear drifts in the maximum Northern Hemisphere overturning and in the volume-averaged ocean temperature over the last 50 years of fully coupled integration are summarized in Table 1 for all simulations.

[16] Owing to the natural variability on timescales as long as 50–100 years, it is difficult to quantitatively estimate the error that is made when using the quasi equilibrium state (last 25 years of simulation) instead of a real equilibrium state. This is particularly true for the maximum overturning strength. For the volume-averaged ocean temperature, the fluctuations are much weaker which allows us to estimate the total error in this quantity. When integrating the model for long times, the drift in the volume-averaged ocean temperature is slowly decreasing, indicating that the model converges toward an equilibrium state. We use this decrease here to estimate the error that we make by using the quasi-equilibrium state at the end of the simulations. We fit a function of the form

$$T_c - A\tau \exp\left(-\frac{(t - t_0)}{\tau}\right), \quad (1)$$

with the parameters T_c as constant part, A as amplitude and τ as timescale to the time series of the volume-averaged temperature $T_{\text{vol.av.}}(t)$. (Here t_0 is 120 years for the Oligocene and present-day simulations, and 340 years for the Miocene simulation.) The fit differs from the real time series by no more than 0.5% for all simulations. Assuming that this time evolution also holds for further time integration of the model, the difference between the temperature T_1 at the end of the simulation (at time t_1) and the final equilibrium temperature T_∞ (at $t = \infty$) is then

$$\Delta T_{\text{vol.av.}} = T_1 - T_\infty = -A\tau \exp\left(-\frac{(t_1 - t_0)}{\tau}\right). \quad (2)$$

The errors in the volume-averaged temperature $T_{\text{vol.av.}}$ estimated from (2), are included in Table 1 for all simulations. The largest error occurs in the Oligocene

Table 1. Model Drift Over the Last 50 Years of Fully Coupled Simulation of the Spin-up Procedure for all Simulations^a

	Oligocene	Miocene	Modern Control	High CO ₂ Modern Control
Trend in the maximum overturning strength in the Northern Hemisphere, Sv/year	−0.012	−0.007	−0.06	−0.078
Trend in the volume-averaged ocean temperature, °C/year	0.0012	0.0018	5×10^{-7}	0.0009
Estimated total error $\Delta T_{\text{vol.av.}}$ in the volume-averaged ocean temperature, °C	0.29	0.14	1.7×10^{-4}	0.10

^aFor the Oligocene and modern control simulations we have used years 270–320, and for the Miocene simulation we have used years 385–435 to calculate the linear drift (first two rows). The last row shows the total error estimate in the volume-averaged ocean temperature as calculated from equation (2). For the exponential fit (equation (1)) we have used years 120–320 for the Oligocene and modern control simulations, and we have used years 340–435 for the Miocene simulation.

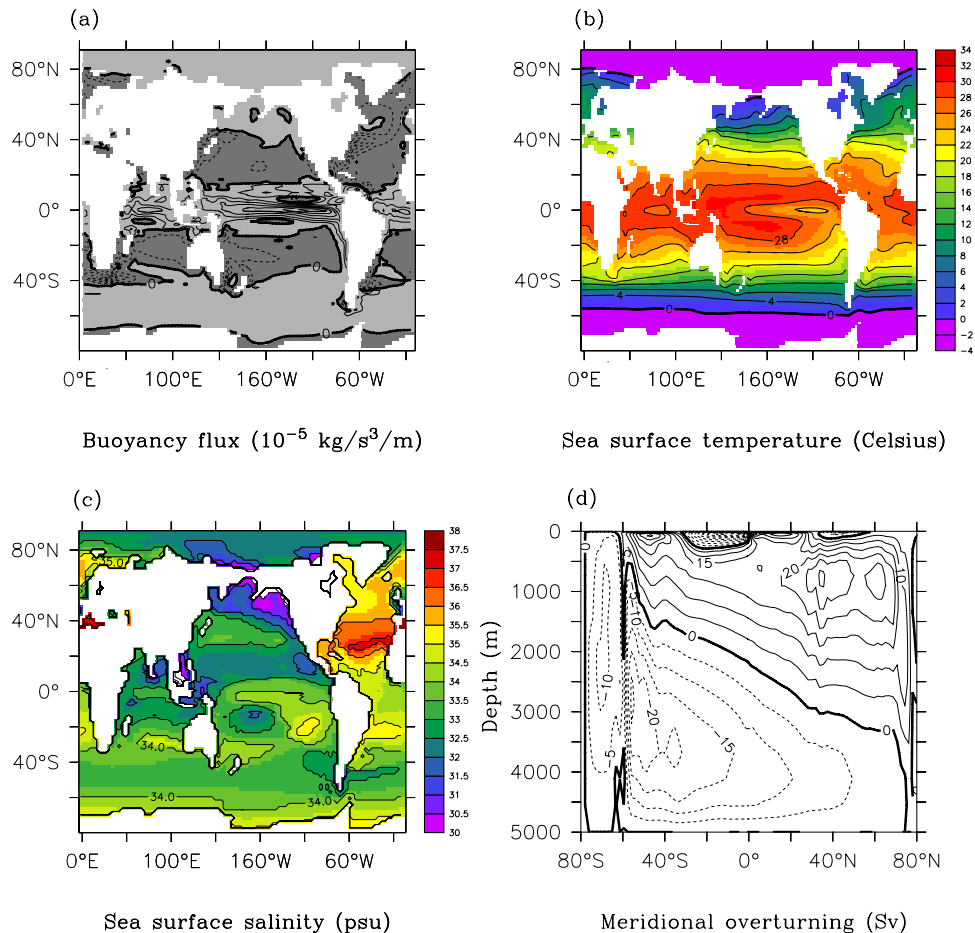


Figure 2. Results of the modern control simulation (with present-day continental geometry and preindustrial atmospheric CO_2 concentration, i.e., $p\text{CO}_2 = 280 \text{ ppmv}$). Data are annual mean values averaged over the last 25 years of simulation. (a) Atmosphere-ocean buoyancy flux field. Dark grey shaded areas indicate negative buoyancy flux; that is, the surface waters become denser there. Contour intervals are $2 \times 10^{-5} \text{ kg s}^{-1} \text{ m}^{-2}$. (b) Sea surface temperature. Contour intervals are 2°C . (c) Sea surface salinity. (d) Global meridional overturning stream function. Dashed lines indicate negative stream function (i.e., counterclockwise circulation). Contour intervals are 5 Sv.

simulation and is 0.29°C . This is still smaller than the temperature differences between the simulations that are discussed in section 4.1. Note also, that the errors due to drift in the sea surface temperature are much smaller than for the volume-averaged temperature.

2.3. Control Simulations

[17] As we use different continental geometries, idealized boundary conditions, and atmospheric CO_2 levels different from present day in our simulations of the Oligocene and Miocene climates, we have performed two control simulations with modern continental geometry.

[18] In the first control simulation we use present-day continental geometry and the preindustrial level of atmospheric CO_2 concentration, i.e., $p\text{CO}_2 = 280 \text{ ppm}$. This simulation will be referred to as modern control simulation. We impose the same idealized boundary conditions, i.e., a flat-bottomed ocean of 5000 m depth, flat land (350 m high) and zonally constant idealized land surface types. As for the

Oligocene/Miocene simulations, we start the ocean model with a zonally constant SST profile, here varying from 28°C at the Equator to 0°C at the poles and a deep sea temperature of -1°C , constant salinity and zero velocity. Initial conditions for the atmosphere are also zonally constant, and the initial sea ice concentration is zero. The spin-up procedure described in section 2.2 is used.

[19] The simulated buoyancy forcing pattern from the atmosphere to the ocean (Figure 2a) agrees well with observations and earlier CCSM simulations with more realistic bathymetry [Doney *et al.*, 1998]. In the tropics and subtropics, the ocean model receives more heat than observed because of an underestimation of the stratus cloud cover by the atmosphere model.

[20] The simulated sea surface temperatures (SSTs) reproduce the observed pattern of SST within errors of $\sim 2^\circ\text{C}$ over much of the ocean (Figure 2b). Larger errors occur in upwelling regions and in high latitudes. The model is too warm by $2^\circ\text{--}6^\circ\text{C}$ along the western coasts of North Amer-

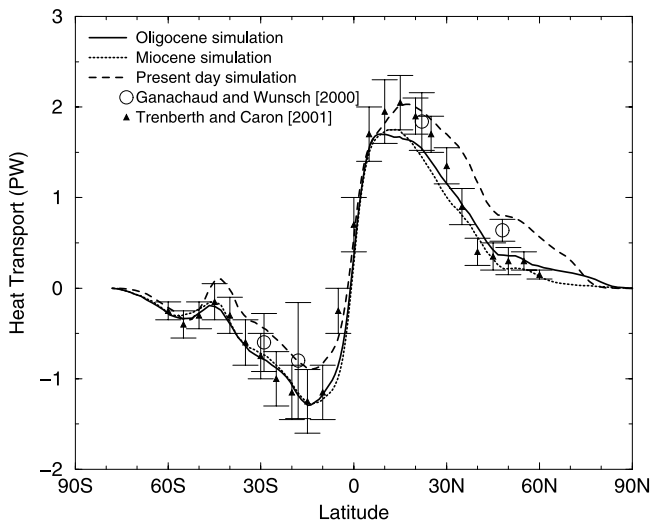


Figure 3. Meridional heat transport by the ocean as simulated by the Community Climate System Model for the late Oligocene (solid line), early Miocene (dotted line), and modern control (dashed line). Data are annual mean values averaged over the last 25 years of simulation. Triangles and circles indicate estimates of the heat transport from observational data from *Trenberth and Caron* [2001] and *Ganachaud and Wunsch* [2000], respectively.

ica, South America, and Africa, because upwelling is underestimated in the ocean model [*Boville and Gent*, 1998; *Otto-Bliesner et al.*, 2002]. On the other hand, the simulated SSTs are too cold (2° – 6° C) in the Southern Ocean, in particular along sea ice margins. The observed sea surface salinity (SSS) pattern is reasonably well reproduced except in the tropical Pacific, where surface waters are too fresh (Figure 2c).

[21] The simulated meridional overturning circulation pattern captures the observed structure with a large overturning cell in the Northern Hemisphere underlain by an overturning cell in the Southern Hemisphere (Figure 2d). Maximum northern overturning rates are 25 Sv at 50° – 60° N and 1500 m depth. The CCSM overestimates the deepwater formation rate in the Northern Hemisphere because of too much sea ice and unrealistic river inflow [*Doney et al.*, 1998; *Otto-Bliesner et al.*, 2002]. The overturning cell in the Southern Hemisphere reaches a maximum of 20 Sv. The model tends to overestimate Antarctic bottom water formation [*Bryan*, 1998]. The meridional heat transport by the ocean in the present-day simulation agrees reasonably well with estimates of the present-day ocean heat transport [*Trenberth and Caron*, 2001; *Ganachaud and Wunsch*, 2000]; see Figure 3. In the Northern Hemisphere, the northward heat transport extends farther north than indicated by observations, probably because of the flat bottom approximation which allows the meridional overturning cell to extend too far north. In the Southern Hemisphere, the southward heat transport is at the lower boundary of the range of estimates from observations.

[22] The idealization of the flat bottom geometry has some disadvantages in simulating realistic flows. The transport of

most of the currents, the ACC in particular, is overestimated as there is no bottom form stress and no topographic steering. When comparing the wind-driven circulation of our present-day control run with a present-day CCSM 1.4 simulation with bottom topography [*Selten et al.*, 2003], it turns out that the subtropical and subpolar gyres in the basins differ slightly in shape, as topography steers them into different areas. However, the global pattern of the wind-driven circulation is very similar in the two cases. The strength and pattern of the thermohaline circulation in the present-day control run, is, however, similar to a present-day simulation which includes bottom topography [*Selten et al.*, 2003].

[23] The assumption of a flat land surface affects mostly the global wind pattern. However, comparing the wind field of our control simulation with a present-day CCSM 1.4 simulation with topography [*Selten et al.*, 2003] shows that most of the differences in the wind field are restricted to land areas and therefore do not significantly affect the wind driven ocean circulation.

[24] The second control simulation is performed in order to distinguish between the effects of (1) atmospheric CO_2 concentration and (2) continental geometry on the thermohaline circulation. This simulation is equal to the first control simulation except for the atmospheric CO_2 concentration which is set to 710 ppm as in the Oligocene and Miocene simulations. It will be referred to as high CO_2 modern control simulation. Sea surface temperatures are in general higher than in the present-day control experiment with lower CO_2 concentration; see Figure 4b. Sea surface salinities are everywhere higher except in the Southern Ocean (ACC region) and in northern high latitudes (north of 75° N) where the surface waters are fresher; see Figure 4c. There are also several differences in the surface buoyancy flux between the two simulations with different atmospheric CO_2 concentration. These differences result from changed precipitation and evaporation patterns and atmosphere-ocean heat flux due to the higher atmospheric CO_2 level. However, the global pattern of surface buoyancy flux, in particular the asymmetry between the North Atlantic and the North Pacific Oceans, does not change due to a higher atmospheric CO_2 concentration. The global meridional overturning is almost the same as in the present-day control simulation with preindustrial CO_2 level; see Figure 4d. This is in agreement with other coupled ocean-atmosphere simulations of the present-day situation which have shown that with a doubled (constant) atmospheric CO_2 level the equilibrium thermohaline circulation is only slightly reduced [*Manabe and Stouffer*, 1994; *Stouffer and Manabe*, 2003]. Even with a quadrupled CO_2 concentration the equilibrium state of the thermohaline circulation remained almost the same [*Stouffer and Manabe*, 2003].

[25] In the rest of the paper we compare the Oligocene and Miocene simulations to the modern control simulation if not stated otherwise.

3. Results

3.1. Fluxes Between the Atmosphere and the Ocean

[26] The ocean circulation is driven by surface momentum fluxes (wind stress) and the fluxes of heat and fresh water. For the Oligocene and Miocene, the simulated annual

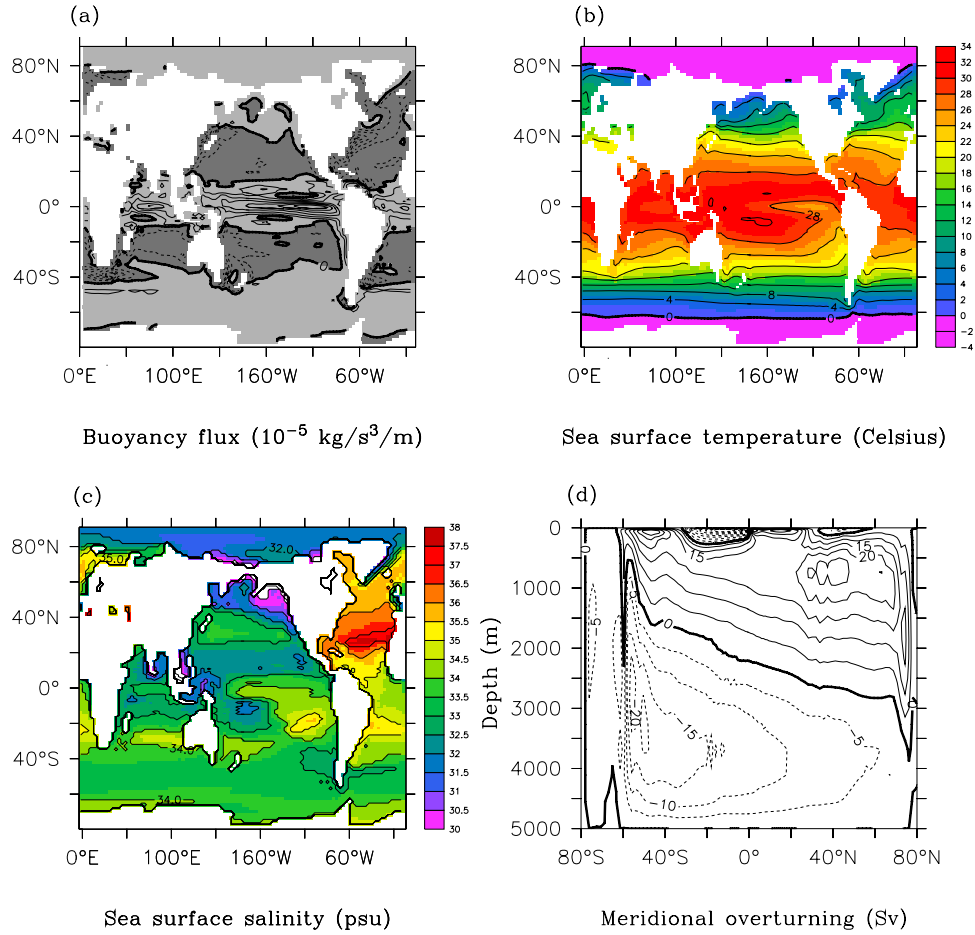


Figure 4. Results of the high CO_2 modern control simulation (with present-day continental geometry and the same atmospheric CO_2 concentration as the Oligocene and Miocene simulations, i.e., $p\text{CO}_2 = 710 \text{ ppmv}$). Data are annual mean values averaged over the last 25 years of simulation. (a) Atmosphere-ocean buoyancy flux field. Dark grey shaded areas indicate negative buoyancy flux; that is, the surface waters become denser there. Contour intervals are $2 \times 10^{-5} \text{ kg s}^{-1} \text{ m}^{-2}$. (b) Sea surface temperature. Contour intervals are 2°C . (c) Sea surface salinity. (d) Global meridional overturning stream function. Dashed lines indicate negative stream function (i.e., counterclockwise circulation). Contour intervals are 5 Sv.

mean wind stress patterns and amplitudes are fairly similar to the present-day winds, with easterlies in the tropics and westerlies at midlatitudes (Figure 5). The slight differences between both fields in Figure 5 are mostly related to local changes in the land-ocean distribution.

[27] Fresh water and heat are exchanged between the ocean and the atmosphere, and both have an effect on the density of the ocean surface waters. The net effect of heat and freshwater fluxes on the surface density is determined by the buoyancy flux, given by

$$B = \frac{1}{c_p} g \alpha Q_{ao} + g \beta (P - E) S_0.$$

Here c_p is the specific heat of water, g the Earth's gravitational acceleration, Q_{ao} the downward heat flux from the atmosphere to the ocean, E the evaporation rate, P the precipitation rate, S_0 the reference salinity used by the

model to calculate the salt flux equivalent to the freshwater flux, α the thermal expansion coefficient of seawater at the surface and β the corresponding expansion coefficient for salinity [Gill, 1982].

[28] The simulated buoyancy flux for both the Oligocene and the Miocene simulations is plotted in Figure 6. The global pattern in both cases is similar to the present-day distributions (Figures 2a and 4a). In the tropics, the ocean surface buoyancy is increased by freshwater input due to net precipitation and by heat input from the atmosphere. At high latitudes, there is negative buoyancy flux and surface waters become denser. One essential difference between the simulated patterns of the different time periods is the contrast between the North Pacific and the North Atlantic Ocean. In the modern control simulation, there is a strong negative buoyancy flux in the North Atlantic extending from about 15°N up to high latitudes (about 80°N). The negative buoyancy flux is particularly strong in the Gulf

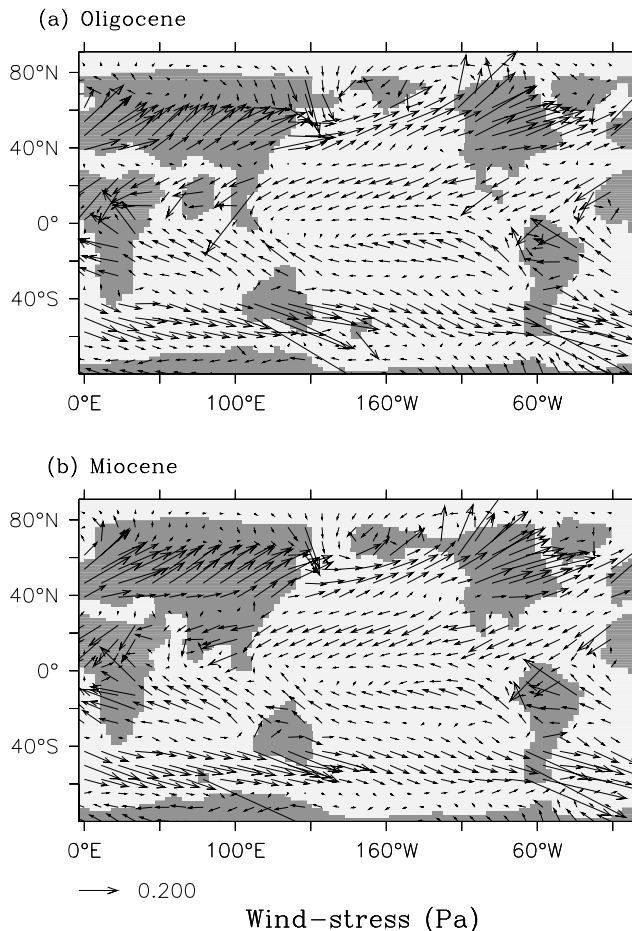


Figure 5. Simulated wind stress field for (a) late Oligocene and (b) early Miocene simulations. Data are annual mean values averaged over the last 25 years of simulation. The wind stress fields are almost equal for both time periods. Also indicated are the continental geometries used in the two simulations.

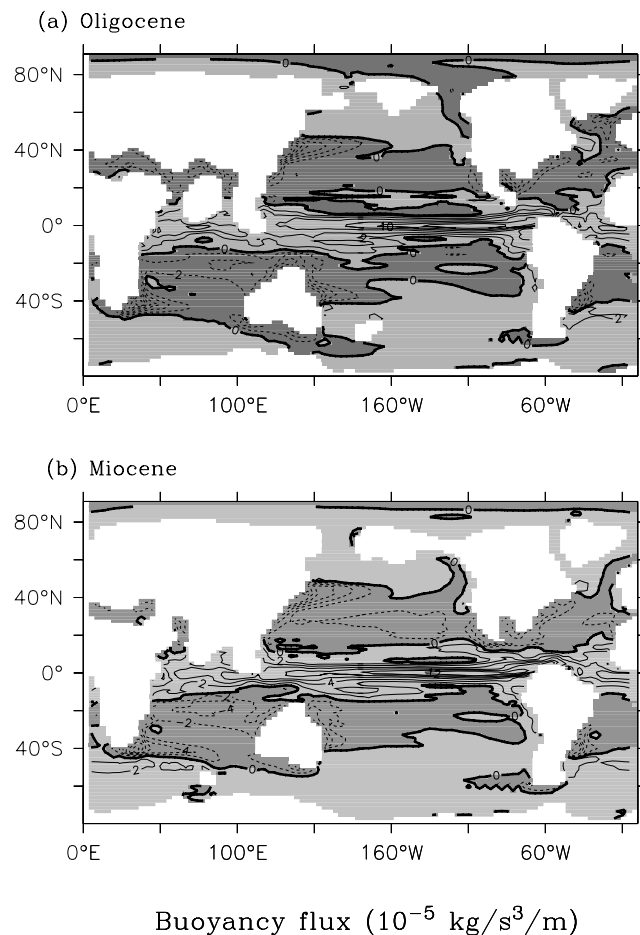
Stream region (Figure 2a). This makes the surface waters in the North Atlantic dense enough for deepwater formation. In the North Pacific there is negative buoyancy flux only in subtropical latitudes. In the Miocene (Figure 6b), the negative buoyancy flux in the North Atlantic is weaker than the present-day flux and it is restricted to lower latitudes (about 15° – 55° N), whereas at high latitudes there is positive buoyancy flux. In the North Pacific, in particular in the Kuroshio region, there is increased heat loss to the atmosphere, and therefore the negative buoyancy flux in that area is stronger than at present. The same is true for the Oligocene simulation (Figure 6a). In addition, in the Oligocene, there is an area of negative buoyancy flux at very high latitudes in the eastern North Pacific, which favors deepwater formation in that area. In the Southern Hemisphere, there are only small differences between the simulations. The forcing fields described above drive the ocean circulation.

3.2. Wind-Driven Ocean Circulation

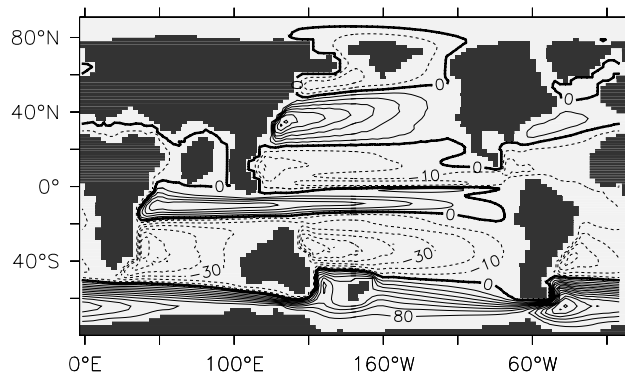
[29] The mostly wind-driven part of the flow is best illustrated by the barotropic stream function which is a

measure of the depth-averaged flow structure. Figure 7 shows the barotropic stream function for the two simulations. Figure 8 shows the surface flow (averaged over the upper 75 m of the water column). In the Oligocene simulation (Figure 7a), there is a northwestward directed current from the Indian Ocean through the Tethys into the Atlantic Ocean, mainly in the southern part of the Tethys. Through the Panama Seaway there is westward flow in the northern part and eastward flow in the southern part, resulting in a weak net westward transport of 3 Sv from the Atlantic into the Pacific Ocean closing the circum-equatorial current. The Antarctic Circumpolar Current (ACC) is constrained by a still relatively small passage between Antarctica and Australia. The transport through Drake Passage is about 90 Sv in the Oligocene simulation. In the Miocene simulation (Figure 7b) the Antarctic Circumpolar Current becomes stronger, as Australia has moved farther northward.

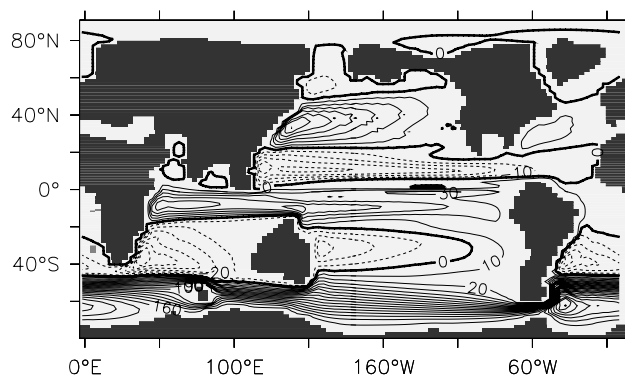
[30] As we have seen in section 2.3, the ACC transport was highly overestimated for the modern control simulation



(a) Oligocene



(b) Miocene



Barotropic stream function (Sv)

Figure 7. Barotropic stream function for (a) late Oligocene and (b) early Miocene simulations. Data are annual mean values averaged over the last 25 years of simulation. Solid lines indicate positive stream function (clockwise gyres); dashed lines indicate negative stream function (anticlockwise gyres). Contour intervals are 10 Sv.

due to the flat bottom idealization. For the Oligocene, we expect that the overestimation of the ACC transport is less severe because the latitude band where unrestricted flow is possible is much smaller than in the present-day continental geometry. Although the absolute value of the ACC transport is certainly overestimated in both the Oligocene and Miocene simulations, a comparison of the three simulations indicates a strong increase in the ACC from the Oligocene through the Miocene to present day.

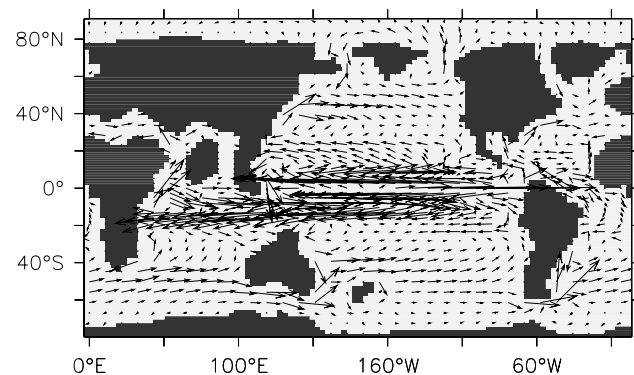
[31] In both the Miocene and Oligocene, western boundary currents developed in all major ocean basins as the poleward flowing part of the subtropical gyres. In the near-tropical region (20°S–20°N) of the Pacific Ocean, two strong gyres just north and south of the equator developed. The southern near-tropical gyre spans both the Pacific and the Indian Ocean. In the Miocene simulation, the southern near-tropical gyre across the Pacific and Indian Oceans increased in strength with respect to the Oligocene simulation and expanded in the meridional direction in the Pacific Ocean. At the same time, the subtropical gyres in the

Southern Hemisphere weakened. In the Northern Hemisphere, the near-tropical gyre in the Pacific Ocean expanded eastward and now spans both the Pacific and the Atlantic Oceans. In the flow field of the upper 75 m, this is reflected in an eastward extension of the North Equatorial Counter Current from the Pacific Ocean into the Caribbean Sea (Figure 8). The eastward flow in the southern part of the Panama Seaway increased compared to the westward flow in its northern part, such that in the Miocene the net transport through this seaway is reversed compared to the Oligocene [von der Heydt and Dijkstra, 2005]. As the African continent has moved toward Eurasia, there is no Tethyan throughflow in the Miocene. In general, the Miocene depth-averaged flow pattern is more asymmetric between the two hemispheres than the Oligocene flow pattern.

3.3. Global Thermohaline Circulation

[32] Sea surface temperatures (SST) in the Oligocene and Miocene simulations (Figure 9) are larger than in the modern control simulation (see Figure 2b). This is partly due to the higher atmospheric CO₂ concentration, compare with Figure 4b. However, in particular in the Southern

(a) Oligocene



(b) Miocene

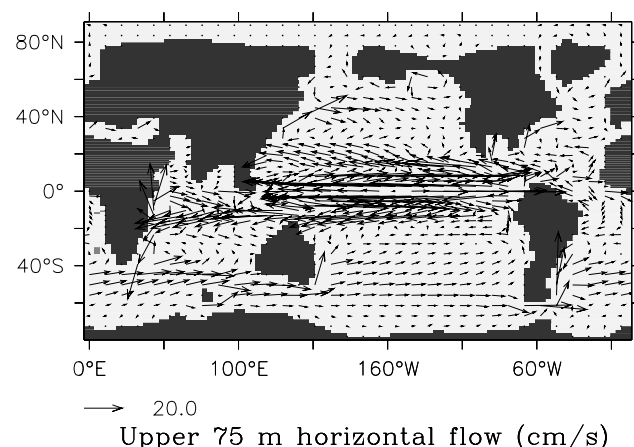


Figure 8. Horizontal flow of the upper 75 m for (a) late Oligocene and (b) early Miocene simulations. Data are annual mean values averaged over the last 25 years of simulation.

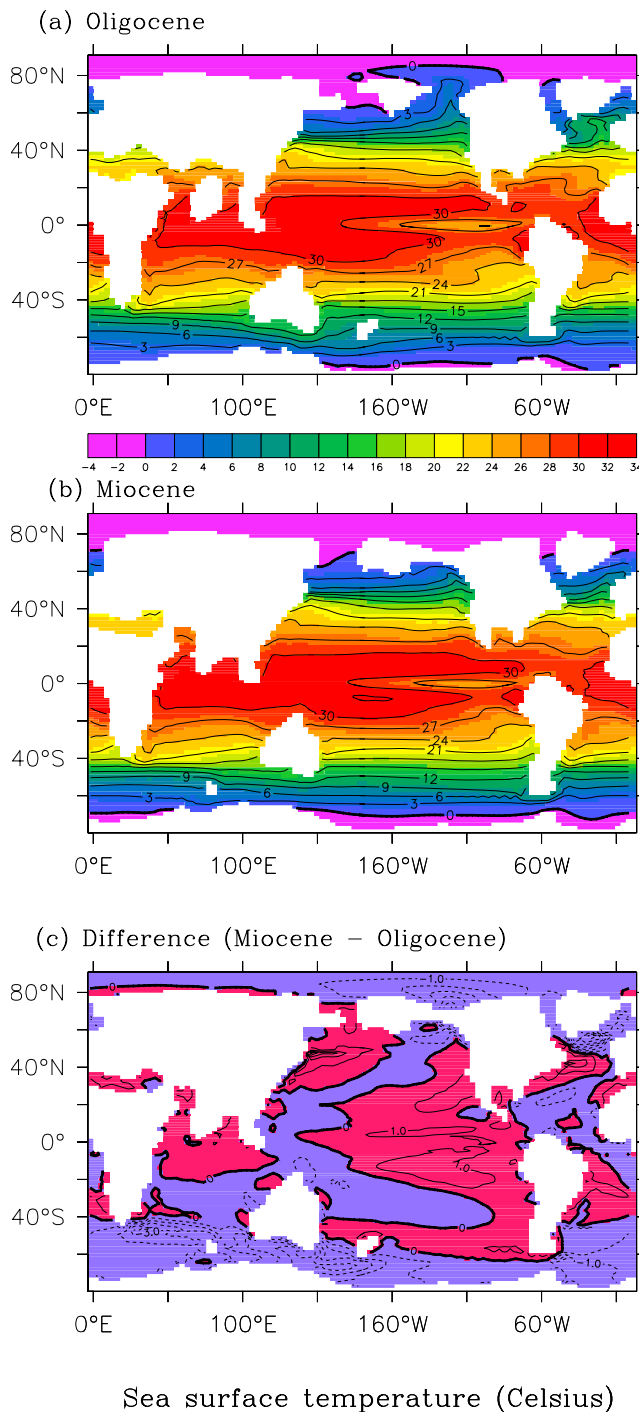


Figure 9. Sea surface temperatures for (a) late Oligocene and (b) early Miocene simulations. Contour intervals are 3°C. (c) Sea surface temperature difference between Miocene and Oligocene simulations. Blue areas indicate areas where it is colder in the Miocene than in the Oligocene. Contour intervals are 1°C. Data are annual mean values averaged over the last 25 years of simulation.

Hemisphere, Oligocene and Miocene SSTs are also larger than in the high CO₂ modern control indicating that the global heat transport is different in the Oligocene and Miocene. The Miocene SSTs are on average lower than those in the Oligocene, in particular at high latitudes. In the Northern Hemisphere, along the western boundary currents in Atlantic and Pacific ocean basins, Miocene SSTs are, however, higher (Figure 9c). As the flow through the Tethys Seaway is blocked in the Miocene, the, now closed to the east, Mediterranean Sea becomes more homogeneous and (on average) warmer. The tropical Atlantic is colder in the Miocene than in the Oligocene.

[33] The sea surface salinity (SSS) is shown in Figure 10 for both Oligocene and Miocene simulations. In the Northern Hemisphere, the Pacific Ocean's surface water freshens from the Oligocene to the present-day situation (compare Figure 10 with Figures 2c and 4c). North of 50°N, Pacific surface salinities in the Oligocene are considerably higher than in the Miocene. On the other hand, in the Miocene, they are still higher than in the high CO₂ modern control simulation. In the Oligocene, the subtropical North Atlantic receives high-salinity water from the westward flowing Tethys current (Figure 7a). The closing of the Tethys connection between the Indian and Atlantic Oceans in the Miocene leads to a strong increase in SSS in the Mediterranean Sea, which can no longer exchange water with the Indian Ocean.

[34] Even though the Tethys was probably not completely closed by 20 Ma [Dercourt *et al.*, 2000], the connection was small and shallow. This was enough to prevent a considerable flow from the Indian to the Atlantic Ocean. Therefore a sea similar to the present Mediterranean with much higher salinities developed and the high-salinity water entered the subtropical North Atlantic. The simulations show that, because of the flow reversal through the Panama Seaway, relatively fresh Pacific water enters the tropical Atlantic Ocean in the Miocene. In contrast to high SSSs in both the high CO₂ modern control and the modern control simulations, SSSs north of 50°N in the North Atlantic remain low in both the Oligocene and Miocene simulations. In the Southern Hemisphere, only minor changes in SSS occur.

[35] From the different patterns of the buoyancy flux, SST, and SSS in the Oligocene, Miocene and control simulations, we can anticipate that the thermohaline circulation (THC) will be different in each of these time slices. In the Oligocene and Miocene simulations, the negative buoyancy flux in the western parts of the Northern Hemisphere subtropical basins is stronger in the Pacific than in the Atlantic. This is in contrast to the present-day pattern, where the evaporation and heat loss to the atmosphere is stronger in the North Atlantic than in the North Pacific.

[36] Indeed, unlike the present-day situation (Figure 4d), the global meridional overturning in both the Oligocene (Figure 11a) and the Miocene (Figure 11b) is much shallower, and the water sinks in the north only down to 1000–1500 m depth. Therefore we refer to it here by intermediate deep water rather than deep water. The northern intermediate deepwater formation rate is about 14 Sv (around 40°–60°N) in the Oligocene and 8 Sv in the Miocene. In the Southern Ocean, there is deepwater formation of subsurface

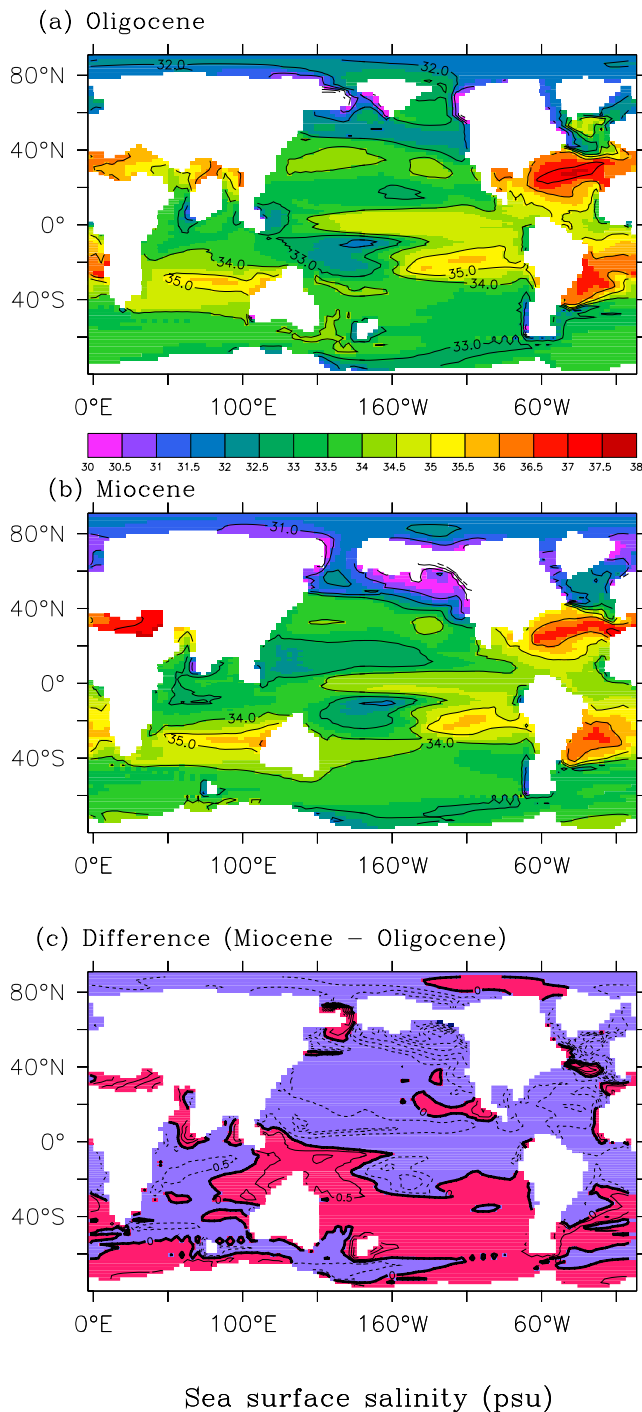


Figure 10. Sea surface salinities for (a) late Oligocene and (b) early Miocene simulations. Contour intervals are 1 practical salinity unit (psu). (c) Sea surface salinity difference between Miocene and Oligocene simulations. Blue areas indicate areas where it is fresher in the Miocene than in the Oligocene. Contour intervals are 0.5 psu. Data are annual mean values averaged over the last 25 years of simulation.

waters. This forms a large (anticlockwise) overturning cell which advects bottom water into the Northern Hemisphere. This southern deepwater formation cell extends farther northward in the Miocene than in the Oligocene.

[37] In the Atlantic Ocean and the Pacific Ocean, substantial changes occur in the meridional overturning going from the Oligocene to the present-day situation (Figure 12). Both modern control simulations display a conveyor type circulation (Figure 12c, high CO_2 modern control not shown), where all deepwater formation in the Northern Hemisphere takes place in the Atlantic Ocean. Instead, in the Oligocene and Miocene, part of the intermediate deep water in the Northern Hemisphere is formed in the Pacific Ocean (Figures 12a and 12b). The Pacific intermediate deepwater formation rate in the Oligocene is about 4 Sv, whereas it is only 2–3 Sv (and shallower) in the Miocene. The other part of the Northern Hemisphere intermediate deep water is formed in the Atlantic Ocean and the Tethys.

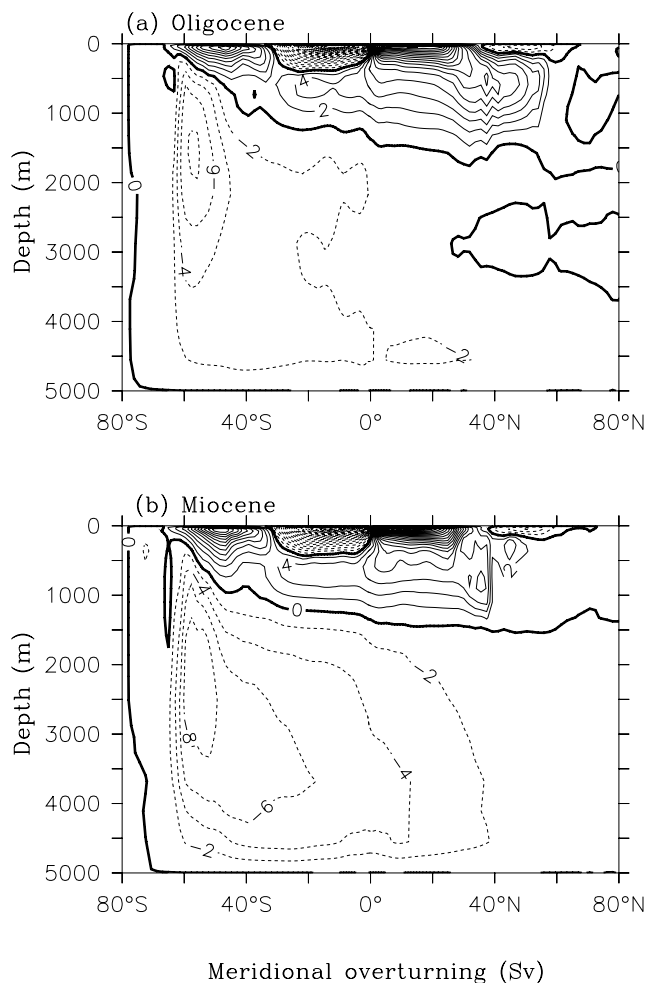


Figure 11. Global meridional overturning stream function for (a) late Oligocene and (b) early Miocene simulations. Data are annual mean values averaged over the last 25 years of simulation. Dashed lines indicate negative stream function (i.e., counterclockwise circulation). Contour intervals are 2 Sv.

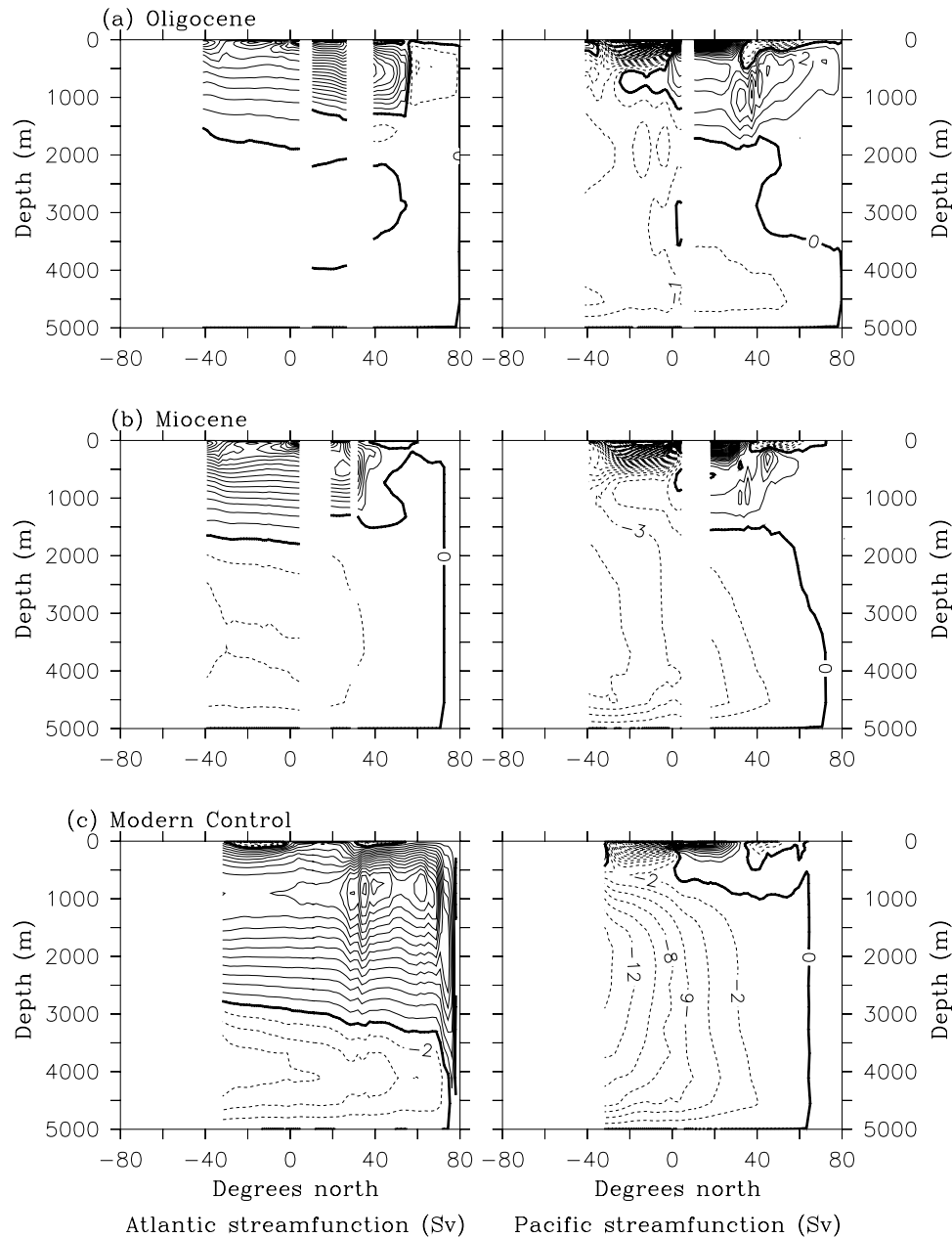


Figure 12. Meridional overturning stream function for the (right) Atlantic and (left) Indo-Pacific oceans. (a) Late Oligocene, (b) early Miocene, and (c) modern control (preindustrial CO_2 level) simulations. Data are annual mean values averaged over the last 25 years of simulation. Dashed lines indicate negative stream function (i.e., counterclockwise circulation). Contour intervals are 2 Sv.

In the Oligocene, deepwater formation in the Atlantic occurs near about 60°N , and about half of this water ($\sim 5\text{--}6$ Sv) flows through the Panama Seaway into the Pacific Ocean and thus does not reach the South Atlantic. In the Miocene, Atlantic intermediate deepwater formation occurs at lower latitudes ($\sim 40^\circ\text{N}$), and most of it reaches the South Atlantic. For both the Miocene and the Oligocene, the Antarctic bottom water that is formed in the Southern Ocean mainly enters the Pacific Ocean and is transported northward at depth. In the Oligocene, this transport is weak

and hardly reaches the Northern Hemisphere. In the Miocene, more Antarctic bottom water flows northward in the Pacific Ocean and partly enters the Atlantic Ocean through the Panama Seaway.

4. Analysis

[38] Section 3 was fairly descriptive and we now analyze two issues in more detail: the physics of the Atlantic-Pacific flow reversal and the thermohaline circulation changes.

Table 2. Volume Transport Through the Different Seaways as Calculated From the Simulations^a

	Volume Transport, Sv	
	Oligocene	Miocene
Φ_D	91.0	146.8
Φ_T	-12.2	0
Φ_P	-4.2	16.8
$\Phi_T + \delta\Phi_D + \delta_\tau$	-4.6	13.3
δ_τ	2.4	1.4

^aDefinitions are Φ_D , Drake Passage transport; Φ_T , Tethys transport; and Φ_P , Panama Seaway transport. Positive values mean eastward transport; negative values indicate westward transport. The fourth row gives the left-hand side of equation (3) and should be compared to Φ_P . The last row shows the contour integral of the wind stress field; see text for explanation.

4.1. Panama Seaway Flow Reversal

[39] As we have seen, the net volume transport through the Panama Seaway reversed direction, from westward flow in the Oligocene to eastward flow in the Miocene. This flow reversal was also found in simulations of the wind-driven flow using a 1.5-layer shallow-water model [Omta and Dijkstra, 2003]. Further analysis of Omta and Dijkstra [2003] showed that the transport through the Panama Seaway was linearly related to the transport through both the Tethys Seaway and Drake Passage.

[40] If the transport through the Panama Seaway is indicated by Φ_P (positive corresponds to eastward transport), that through Drake Passage is indicated by Φ_D and that through the Tethys Seaway is indicated by Φ_T , then this relation is given by

$$\Phi_P = \Phi_T + \delta\Phi_D + \delta_\tau, \quad (3)$$

where

$$\delta = \frac{\sin \theta_{SA} - \sin \theta_D}{\sin \theta_S - \sin \theta_{SA}} \quad (4)$$

is a geometrical factor. This factor involves the latitude halfway through Drake Passage θ_D , the latitude of the northern edge of South America θ_S , and the latitude halfway between Antarctica and South Africa θ_{SA} . The quantity δ_τ is given by

$$\delta_\tau = \frac{1}{2\Omega\rho_0(\sin \theta_{SA} - \sin \theta_S)} \int_C \boldsymbol{\tau} \cdot \mathbf{ds}. \quad (5)$$

[41] Here Ω is the angular frequency of the Earth, ρ_0 is the mean density of seawater and $\boldsymbol{\tau}$ is the wind stress vector. The contour C connects the eastern African coast with the northern edge of South America and then continues along the eastern coast of South America to its southern tip, crosses Drake Passage, and reaches the coast of Antarctica. It follows eastward along the Antarctic coast, connects from there to the tip of South Africa, and, finally, closes with its starting point on the east coast of Africa [Omta and Dijkstra, 2003].

[42] From (3), we see that as long as the westward transport through the Tethys Seaway is large enough ($\Phi_T < 0$) and

the eastward transport through Drake Passage is not too strong ($\Phi_D > 0$), the flow through the Panama Seaway is dominated by the Tethys transport and is westward, ($\Phi_P < 0$). With decreasing strength of the Tethys current, however, and increasing ACC transport, the Panama Seaway transport becomes smaller and smaller, and finally reverses as the ACC becomes strong enough.

[43] The relation (3) was derived in the very simplified context of a shallow-water model and hence there is no a priori reason why it should hold in the CCSM simulations. In Table 2, the relevant transports calculated from both Oligocene and Miocene simulations are presented. The value of the wind stress integral δ_τ is varying between 1.4 and 2.4 Sv in the two simulations. In the fourth row of Table 2, the value of Φ_P based on (3) is presented and these values match very well with the values directly computed from the simulations (third row in Table 2).

[44] For the Oligocene simulation, the transport through the Panama Seaway, as predicted from (3), is 9% larger than the calculated transport. For the Miocene simulation, the relation (3) underestimates the simulated transport Φ_P by 20%. The deviations between simulated transport and that derived from (3) result from the simplifications that are made in the derivation of equation (3).

[45] In both simulations, the prevailing winds in the Caribbean are easterlies (Figure 5). Therefore the mean surface flow in the ocean through the Panama Seaway is westward in the Oligocene as well as in the Miocene. Figure 13 shows the vertical and meridional structure of the zonal velocity in the Panama Seaway, averaged from 75°W to 65°W. Positive zonal velocities denote eastward flow. In the southern part of the Caribbean Sea (around 6°N), there is an eastward current below the surface with its maximum (eastward transport) at a depth of about 100 m. This subsurface current strongly increases in strength from the Oligocene to the Miocene, and is an eastward extension of the north equatorial counter current in the Pacific Ocean. This leads to a net eastward flow across the Panama Seaway in the Miocene. It brings cool and low-salinity water into the Atlantic, which cools the Caribbean Sea [von der Heydt and Dijkstra, 2005], and leads to lower salinities by about 0.8 psu in the upper 800 m of the tropical Atlantic (Figures 14a and 14b).

[46] In the northern part of the Caribbean Sea (~14°–20°N) there is westward flow in both time periods. In the Oligocene, this is mainly water coming from the Tethys Ocean which is crossing the Atlantic Ocean. Part of the shallow deep water formed in the North Atlantic also flows into the Pacific here. In the Miocene, westward velocities in the northern part of the Caribbean Sea are of the same magnitude, but are confined to the upper 400 m only. In general, the zonal westward flow across the Atlantic is much less in the Miocene due to the closure of the Tethys Seaway. Farther north in the cross section of Figure 13, there is again eastward flow in both time periods. This can be attributed to the beginning of the western boundary current along the coast of North America (see Figures 7 and 8).

[47] As we have noted in section 2.3 the currents are in general overestimated in our simulations due to the flat bottom approximation. Therefore, if the bottom topography

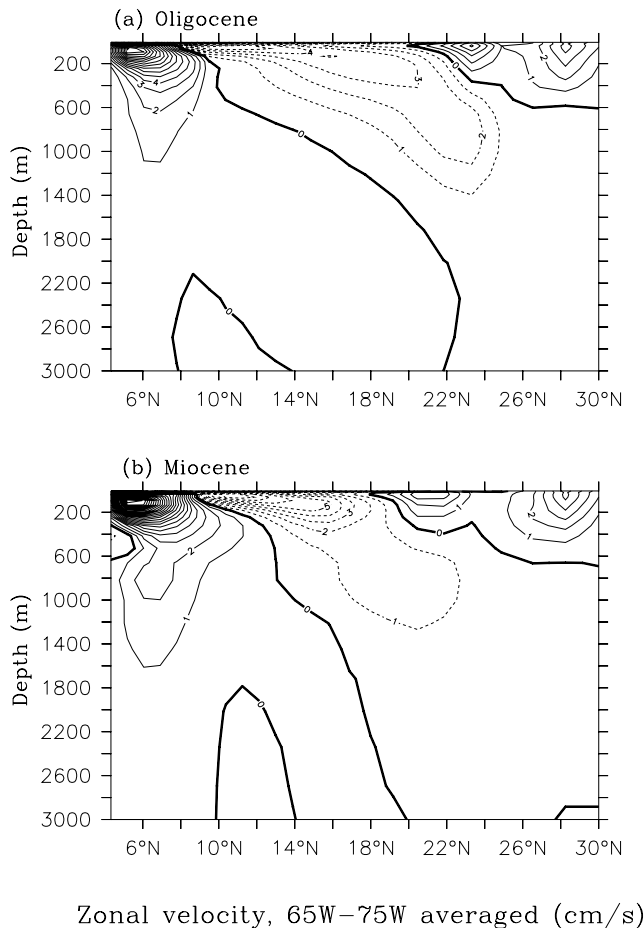


Figure 13. Isolines of the zonal velocity in the Panama Seaway as a function of depth and latitude. The velocity is averaged from 75°W to 65°W. (a) Late Oligocene and (b) early Miocene. Data are annual mean values averaged over the last 25 years of simulation. Solid contours indicate positive, i.e., eastward velocities; dashed lines mean westward velocities. Contour intervals are 1 cm s^{-1} .

of both the 30 Ma and 20 Ma situations were accurately known, it should have been included; these bathymetries are, however, not well known. The flat bottom CCSM configuration is therefore a better next step from a 1.5-layer shallow-water model to test whether a Panama flow reversal can occur due to gateway changes than two cases with highly uncertain bottom topography. As the global pressure field is substantially influenced by bathymetry, it is much more difficult in the latter case to distinguish the effects of changing continental geometry and bottom topography.

[48] In addition, the overestimation of the currents in the flat bottom case will not affect the occurrence of the flow reversal. As the relation (3) indicates, it is the increase in Drake Passage transport (Φ_D) together with the decrease in Tethys transport (Φ_T) that causes the flow reversal. Even if Φ_D and Φ_T were smaller because of the presence of bottom topography, the tendencies in both quantities with time would be similar, and hence only the timing of the reversal would be affected, not its existence. We consider the

addition of bottom topography as a next step in the analysis of flows in the Oligocene and Miocene configurations. In this way, the flat bottom case serves as a reference to study the effects of specific features in the bottom topography and their effect on the global pressure field.

[49] Because the transports as calculated from our simulations match relatively well the relation (3), we conclude that the flow reversal through the Panama Seaway is mainly induced by changes in the wind-driven circulation. Those, in turn, are determined by the changes in the continental configuration which affect the global horizontal pressure gradient fields as given by *Omta and Dijkstra* [2003].

[50] The circulation patterns computed are qualitatively consistent with previous model results. Earlier model experiments with an ocean general circulation model with present-day continental geometry have indicated that, with an open Panama Isthmus, low-salinity waters from the Pacific enter the Atlantic Ocean through the Panama Seaway [*Maier-Reimer et al.*, 1990], i.e., eastward flow through the Panama Seaway is observed. This simulation corresponds to a situation before 3–4 Ma, when the continental geometry was close to present day, but the Panama Seaway was open. Other ocean model simulations [*Nisancioglu et al.*, 2003] with present-day geometry and an open Panama Seaway show eastward flow from the Pacific to the Atlantic in the upper layers. They find, in addition, that a substantial amount of North Atlantic deep water is exported to the Pacific Ocean through a deep open Panama Seaway. Also, in coupled ocean-atmosphere model experiments with an open Panama Seaway, eastward flow through the seaway from the Pacific to the Atlantic Ocean has been found [*Murdock et al.*, 1997; *Prange and Schulz*, 2004]. The eastward transport through the Panama Seaway of 15.6 Sv that has been found by *Murdock et al.* [1997] is even in close agreement with our Miocene simulation. Climate model simulations for earlier time periods, i.e., for the Eocene [*Huber and Sloan*, 2001; *Huber et al.*, 2003] and the Cretaceous [*Bush and Philander*, 1997; *Otto-Bliesner et al.*, 2002], where the continental geometry is very different from present day and the Tethys Seaway is much wider than in our Oligocene simulations, all indicate a westward circumequatorial current, i.e., transport from the Atlantic into the Pacific through the Panama Seaway.

[51] Although it is difficult to present a good data-model comparison, available proxy data seem to be qualitatively in agreement with the computed flow patterns. Oxygen isotope records from the eastern equatorial Atlantic (ODP Site 926/929) indicate an increase in the $\delta^{18}\text{O}$ of planktonic foraminifera of $\sim 0.25\text{‰}$ between times before and after the Oligocene/Miocene boundary [*Paul et al.*, 2000]. To compare our results with these values, we have calculated the oxygen isotopic composition that a calcite sample would have from the simulated temperatures and salinities in the equatorial Atlantic. The oxygen isotopic composition of seawater δ_w is calculated by the empirical relation between δ_w and salinity [*Broecker*, 1989]. The seawater isotopic composition together with the simulated temperature of the upper 100 m in the ocean is then used to calculate the calcite isotopic composition according to the calcite-temperature relation of *Erez and Luz* [1983]. Assuming similar ice

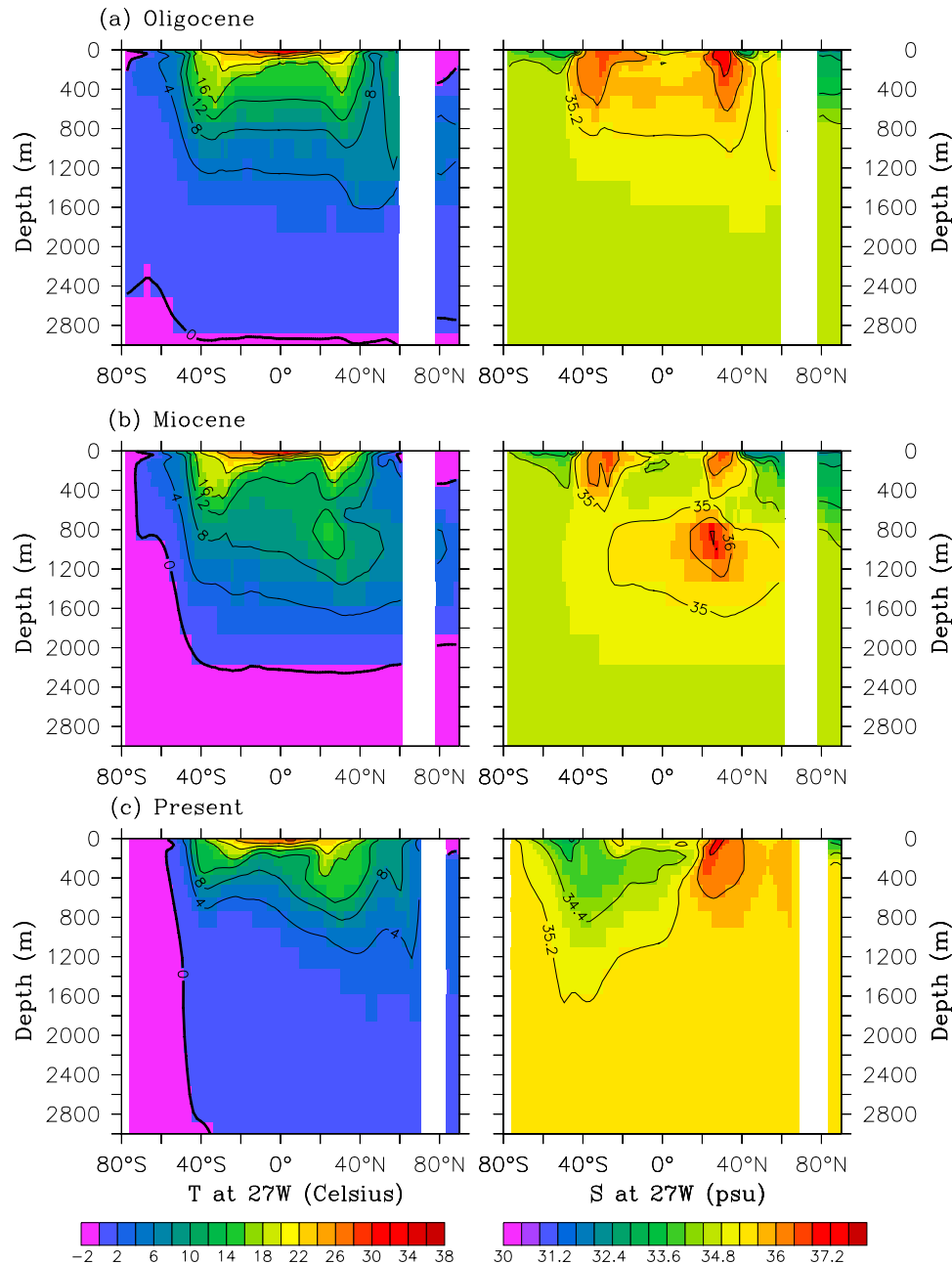


Figure 14. Latitude-depth cross sections of the simulated (left) ocean temperatures and (right) salinities at 27°W (Atlantic Ocean). (a) Late Oligocene, (b) early Miocene, and (c) modern control (preindustrial CO₂ level) simulations. Data are annual mean values averaged over the last 25 years of simulation. Contour intervals in the temperature plots are 4°C, and in the salinity plots they are 0.8 psu.

volumes, the resulting difference in calcite $\delta^{18}\text{O}$ between the Miocene and the Oligocene simulations at the location of ODP Site 926/929 is then 0.12‰. To the north of that site, the increase of $\delta^{18}\text{O}$ values is more pronounced. The strongest increase in $\delta^{18}\text{O}$ calculated from the simulations occurs to the northeast of South America (47°–53°W, 3°–8°N; 0.32‰).

[52] A study of the sedimentation rates in the tropical Pacific [Moore *et al.*, 2004] during the last 56 Myr indicates a different pattern of sedimentation in the eastern tropical Pacific before and after about 30 Ma. In the older records,

there are tongues of high accumulation rates to the north and south of the equator, which are not found in the records after 30 Ma. This may indicate flow reorganizations in that area. Our simulations suggest that, at that time, less water was entering the tropical Pacific from the Atlantic and Tethys Oceans; since the flow reversal in the Panama Seaway in the early Miocene, increased transport of Pacific water into the Atlantic has occurred. Wade and Pälike [2004] find an increase in planktonic $\delta^{18}\text{O}$ values at ODP site 1218 in the tropical Pacific around 26 Ma. This site lies within the

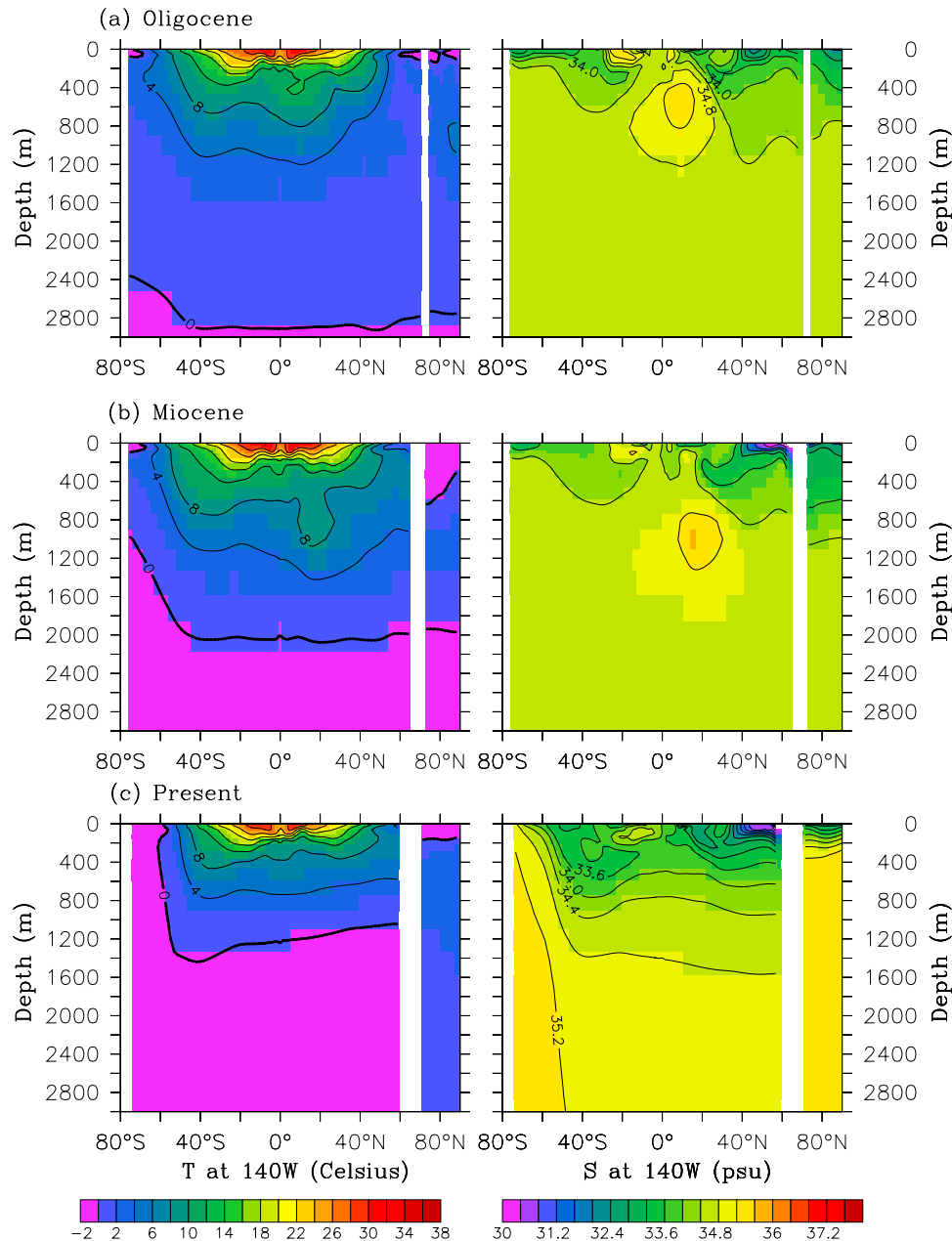


Figure 15. Latitude-depth cross sections of the simulated (left) ocean temperatures and (right) salinities at 140W (Pacific Ocean). (a) Late Oligocene, (b) early Miocene, and (c) modern control (preindustrial CO₂ level) simulations. Data are annual mean values averaged over the last 25 years of simulation. Contour intervals in the temperature plots are 4°C and in the salinity plots 0.8 psu.

area of the North Equatorial Counter Current (NECC) and may therefore record our simulated increase in the NECC from the Oligocene to the Miocene. At that site, we find only a small temperature decrease in the upper 200 m but the cooling is much stronger slightly to the east of that site.

4.2. Thermohaline Circulation Changes

[53] The thermohaline circulation in the Oligocene and Miocene simulations is substantially different from the present-day circulation. To determine the cause of these changes, we analyze the temperature and salt distributions

in the ocean basins for the different periods. Latitude-depth cross sections of temperature and salinity through the Atlantic (27°W) and the Pacific Ocean (140°W) are shown in the Figures 14 and 15, respectively. In the modern control simulation, the downward sloping of the Atlantic isotherms from south to north and the steep isotherms and isohalines north of 50°N indicates that relatively high density water sinks in northern high latitudes to about 3000 m depth. This water fills the South Atlantic (Figure 14c) and it is underlain by colder Antarctic Bottom Water. In the Pacific Ocean, no deep water is formed because the surface waters are much

fresher (Figure 15c). The strong salinity difference between the Atlantic and the Pacific Ocean is maintained because the two basins are connected only at southern high latitudes.

[54] In the Oligocene and Miocene continental geometries, there are, in addition to a southern connection, connections between the two basins at low latitudes. In the Oligocene, the westward flowing circumglobal Tethys current redistributes salt between the Atlantic and the Pacific. The steep isotherms in the 140°W section north of 45°N (Figure 15a) indicate that deepwater formation occurs in the North Pacific; it is, however, only sinking to intermediate depths (Figure 11a). The same holds for the Oligocene Atlantic Ocean; see Figure 14a. In contrast to the present-day overturning circulation, the meridional overturning in the Oligocene is more symmetric between the Atlantic and the Pacific. This is due to the smaller salinity contrast between the two basins.

[55] In the Miocene, the global meridional overturning circulation is similar to the Oligocene (Figure 11). From the cross sections at 140°W (Figure 15b), it appears that there is less Pacific deepwater formation in the Miocene than in the Oligocene. This is because the surface salinities north of 45°N in the Pacific are much lower. In the Oligocene, salty water is continuously redistributed between the Atlantic and Pacific Oceans by the currents in the circumequatorial seaway. In particular, relatively salty water from the tropical Atlantic enters the Pacific through the Panama Seaway. This may lead to higher SSSs in the North Pacific. In the Miocene, there is no circumequatorial flow, and, in addition, due to the flow reversal in the Panama Seaway, there is no more input of salty water from the tropical Atlantic. This leads to lower SSSs in the North Pacific. Furthermore, low-salinity Pacific water reduces the salinity of the tropical Atlantic (Figure 14b) in the Miocene. This indicates, that the ocean connection through the Panama Seaway is still sufficient to prevent the buildup of a strong salinity contrast between the Atlantic and the Pacific Oceans as in the present-day situation (compare with the two modern control simulations). The northward branch of the thermohaline circulation therefore remains shallow in the Miocene as well.

[56] The high-CO₂ modern control simulation, i.e., with the same high atmospheric CO₂ level as the Miocene and Oligocene simulations, has revealed that the thermohaline circulation is basically the same as in the modern control experiment with preindustrial CO₂ level, i.e., a conveyor type circulation with strong deepwater formation in the North Atlantic and a more or less passive Pacific Ocean. The strength of the overturning cell in the Southern Hemisphere is only slightly reduced as compared to the present-day simulation with preindustrial CO₂ concentration. The higher atmospheric CO₂ concentration does not influence the salinity contrast between Atlantic and Pacific Ocean as can be seen by comparing the two modern control simulations (Figures 2c and 4c). Therefore the different thermohaline circulation patterns that we find in the Oligocene and Miocene simulations cannot be explained by the higher atmospheric CO₂ level. Instead, this indicates that the changes in the thermohaline circulation from the Oligocene to the present-day simulations are mostly due to tectonic changes.

[57] Owing to shallower meridional overturning circulations in both the Oligocene and Miocene, the poleward heat

transport by the ocean in the Northern Hemisphere is reduced compared to that of the modern control simulation (Figure 3). The heat transport is, however, increased in the Southern Hemisphere. Maximum poleward heat transport in the Oligocene/Miocene simulations is 1.7 PW in the Northern Hemisphere, which is 0.4 PW smaller than in the present day case, and 1.3 PW in the Southern Hemisphere; the latter is 0.5 PW larger than the present-day value.

[58] The shallow overturning circulation found in the North Atlantic in both the Oligocene and Miocene simulations is in agreement with proxy data studies. *Paul et al.* [2000] find a weak south to north $\delta^{13}\text{C}$ gradient in benthic foraminifera data in the early Miocene Atlantic Ocean, with the heaviest $\delta^{13}\text{C}$ values in the South Atlantic. This indicates that Southern Ocean deep waters were filling the deep (3000–4000 m) Atlantic from the south, and northern deep water was absent or shallow. *Billups et al.* [2002] concluded from benthic foraminifera $\delta^{18}\text{O}$ gradients between the North and South Atlantic that, in the late Oligocene and early Miocene, a relatively warm deepwater mass forming in the North Atlantic reached the deep tropical Atlantic but not the South Atlantic. This is consistent with our late Oligocene simulation, which indicates that a part of the shallow deep water from the North Atlantic flows through the Panama Seaway into the Pacific Ocean. Deep water Nd isotope ratios from the western tropical Pacific decrease from radiogenic values at 38 Ma toward more nonradiogenic values at 17 Ma indicating that more and more Southern Ocean deep water was reaching the tropical Pacific with time [*van de Flierdt et al.*, 2004]. In our Miocene simulation, more Southern Ocean deep water is formed than in the Oligocene simulation and also flows farther north into the Pacific Ocean.

[59] The changes in the THC become even more interesting when put into context with other model results for different geological time periods. In the CCSM Eocene simulation [*Huber and Sloan*, 2001; *Huber et al.*, 2003], the main sites of deepwater formation are in the northern Atlantic and the Tethys but not in the northern Pacific and there is no Antarctic bottom water formation. However, a simulation started with different initial conditions also showed deep convection in the Southern Ocean. This indicates that there may be multiple equilibria in the CCSM, which we also cannot rule out for our simulations. A completely different meridional overturning circulation state has been found in the Cretaceous simulation within the NCAR CCSM [*Otto-Bliesner et al.*, 2002]. During that time, the continents were distributed much more symmetrically on the two hemispheres, with a wide open ocean connection around the equator. The overturning circulation shows two symmetric overturning cells on each hemisphere, with sinking in the north and upwelling at the equator.

[60] In summary, the presence of gateways exerts a strong influence on the thermohaline circulation because gateways control the interbasin transport of salt.

5. Summary

[61] Using a flat geometry for both ocean and atmosphere and idealized vegetation zones, coupled equilibrium climate

states for the Oligocene (30 Ma) and the Miocene (20 Ma) were calculated with version 1.4 of the CCSM. In addition, two control simulations with present-day continental geometry were performed, one with preindustrial atmospheric CO₂ concentration and another with the same high atmospheric CO₂ concentration as the Oligocene and Miocene simulations. There is still some drift in each of the coupled simulations, but an estimate of the drift in the meridional overturning strength and the volume-averaged ocean temperature indicates that the drift causes only minor errors in the flow and tracer fields. Our analysis focused on the impact of gateway changes on the global wind-driven and thermohaline circulation.

[62] Considering the vertically averaged (mainly wind driven) circulation, we find several major changes between the Oligocene and the Miocene simulations. Because of the closure of the Tethys Seaway and the widening of the Southern Ocean passages, the net volume transport through the Panama Seaway changes sign. In the Oligocene, it is directed from the Atlantic to the Pacific, whereas in the Miocene, a subsurface current from the Pacific to the Caribbean Sea strongly increases and therefore leads to net eastward transport across the seaway. A comparison between the transports simulated here and those derived from an analysis of the results of a 1.5-layer shallow-water model [Omta and Dijkstra, 2003] indicates that the physical mechanism of the reversal of the net volume transport is indeed related to a change in the global (oceanic) pressure distribution associated with the changes in the gateways. Note that this is the only factor which can change the pressure distribution because the bottom topography (i.e., a flat bottom) is the same in each simulation.

[63] The influence of the flow reversal on the large-scale climate seems to be localized mostly to the Caribbean Sea and the tropical Atlantic. The surface waters in that area cool substantially in the early Miocene, and therefore the flow reversal may have induced the demise of Caribbean warm water corals in the early Miocene [von der Heydt and Dijkstra, 2005].

[64] Concerning the thermohaline circulation, it appears that changes in continental geometry can lead to different patterns of the thermohaline circulation. In our simulations,

the Oligocene and Miocene meridional overturning circulation is substantially different from the present-day circulation. We find deepwater formation at high latitudes in both the North Atlantic and the North Pacific, in particular in the Oligocene simulation. This is contrary to the present-day state of deepwater formation in the North Atlantic and a more or less passive Pacific Ocean. The reason for the differences is the gateway control of interbasin exchange of salt which affects the contrast between Atlantic and Pacific and hence the meridional overturning circulation. Because of the similar global meridional overturning circulation in both the Oligocene and the Miocene, the global impact of the flow reversal appears limited. The different flow structure in the Panama Seaway in the Oligocene and Miocene simulations may, however, influence the salinity distribution between the Atlantic and Pacific Oceans as it controls the transport between the two basins. It may therefore contribute to the reduction of deepwater formation in the North Pacific in the Miocene.

[65] These simulations, together with the ones presented in this paper indicate that the THC might have undergone large global changes during the Tertiary. A transition between the different overturning states that have been found in the Late Cretaceous and in our Oligocene/Miocene certainly must have occurred. Furthermore, a transition must have occurred from an overturning state with deepwater formation in both the North Pacific and the North Atlantic to the present-day “conveyor” state with deepwater formation in the North Atlantic only. Were these transitions gradual or relatively fast with respect to timescales of continental motion and were other factors than continental geometry (e.g., atmospheric composition) involved? Further work will have to reveal more about the changes in global ocean circulation patterns and their effect on global climate.

[66] **Acknowledgments.** We thank Michael Kliphuis (KNMI) and Christine Shields (NCAR) for their help to get the CCSM code running. We also thank three anonymous referees and the Editor for very helpful suggestions. All computations were performed at the Academic Computing Center (SARA), Amsterdam. Computer resources were funded under project SC-122 by the National Computing Facilities Foundation (NCF) with financial support from the Netherlands Organization for Scientific Research (NWO).

References

- Barker, P. F., and J. Burrell (1977), The opening of the Drake Passage, *Mar. Geol.*, **25**, 15–34.
- Billups, K., J. E. T. Channell, and J. C. Zachos (2002), Late Oligocene to early Miocene geochronology and paleoceanography from the subantarctic South Atlantic, *Paleoceanography*, **17**(1), 1004, doi:10.1029/2000PA000568.
- Bonan, G. B. (1998), The land surface climatology of the NCAR Community Climate Model, *J. Clim.*, **11**, 1307–1326.
- Boville, B. A., and P. R. Gent (1998), The NCAR Climate System Model version one, *J. Clim.*, **11**, 1115–1130.
- Broecker, W. S. (1989), The salinity contrast between the Atlantic and Pacific oceans during glacial time, *Paleoceanography*, **4**, 207–212.
- Bryan, F. O. (1998), Climate drift in a multicentury integration of the NCAR Climate System Model, *J. Clim.*, **11**, 1455–1471.
- Bush, A. B. G., and S. G. H. Philander (1997), The late Cretaceous: Simulation with a coupled atmosphere-ocean general circulation model, *Paleoceanography*, **12**, 495–516.
- Crowley, T. J., and G. R. North (1991), *Paleoclimatology*, Oxford Univ. Press, New York.
- Danabasoglu, G., J. C. McWilliams, and W. G. Large (1996), Approach to equilibrium in accelerated global oceanic motion, *J. Clim.*, **9**, 1092–1110.
- Dercourt, J., M. Gaetani, B. Vrielynck, E. Barrier, B. Bijou-Duval, M. F. Brunet, J. P. Cadet, S. Crasquin, and M. Sandulescu (2000), *Peri-Tethys Palaeogeographical Atlas*, Comm. for the Geol. Map of the World, Paris.
- Doney, S. C., W. G. Large, and F. O. Bryan (1998), Surface ocean fluxes and water-mass transformation rates in the coupled NCAR Climate System Model, *J. Clim.*, **11**, 1420–1441.
- Edinger, E. N., and M. J. Risk (1994), Oligocene-Miocene extinction and geographic restriction of Caribbean corals - roles of turbidity, temperature, and nutrients, *Palaios*, **9**, 576–598.
- Edinger, E. N., and M. J. Risk (1995), Preferential survivorship of brooding corals in a regional extinction, *Paleobiology*, **21**, 200–219.
- Erez, B., and J. Luz (1983), Experimental paleotemperature equation for planktonic foraminifera, *Geochim. Cosmochim. Acta*, **47**, 1025–1031.
- Ganachaud, A., and C. Wunsch (2000), Improved estimates of global ocean circulation,

- heat transport and mixing from hydrographic data, *Nature*, 408, 453–457.
- Gill, A. E. (1982), *Atmosphere-Ocean Dynamics*, Elsevier, New York.
- Hallam, A. (1969), Faunal realms and facies in the Jurassic, *Paleontology*, 12, 1–18.
- Huber, M., and L. C. Sloan (2001), Heat transport, deep waters, and thermal gradients: Coupled simulations of an Eocene greenhouse climate, *Geophys. Res. Lett.*, 28, 3481–3484.
- Huber, M., L. C. Sloan, and C. Shelitto (2003), Early Paleogene oceans and climate: A fully coupled modeling approach using the NCAR CCSM, *Spec. Pap. Geol. Soc. Am.*, 369, 25–47.
- Kennett, J. P. (1977), Cenozoic evolution of Antarctic glaciation, the circum-Antarctic Ocean and their impact on global paleoceanography, *J. Geophys. Res.*, 82, 3843–3860.
- Kiehl, J. T., J. J. Hack, G. B. Bonan, and B. A. Boville (1998), The National Center for Atmospheric Research Community Climate Model CCM3, *J. Clim.*, 11, 1131–1149.
- Lawver, L. (1992), The development of paleoseaways around Antarctica, in *The Antarctic Paleoenvironment: A Perspective on Global Change*, *Antarct. Res. Ser.*, vol. 56, edited by J. P. Kennett and D. A. Warnke, pp. 7–30, AGU, Washington, D. C.
- Maier-Reimer, E., U. Mikolajewicz, and T. Crowley (1990), Ocean general circulation model sensitivity experiment with an open Central American isthmus, *Paleoceanography*, 5, 349–366.
- Manabe, S., and R. J. Stouffer (1994), Multiple-century response of a coupled ocean-atmosphere model to an increase of atmospheric carbon dioxide, *J. Clim.*, 7, 5–23.
- Miller, K. G., J. D. Wright, and R. G. Fairbanks (1991), Unlocking the ice house: Oligocene-Miocene oxygen isotopes, eustasy, and margin erosion, *J. Geophys. Res.*, 96, 6829–6848.
- Moore, T. C., Jr., J. Backman, I. Raffi, C. Nigrini, A. Sanfilippo, H. Pälike, and M. Lyle (2004), Paleocene tropical Pacific: Clues to circulation, productivity, and plate motion, *Paleoceanography*, 19(1), PA3013, doi:10.1029/2003PA000998.
- Murdoch, T. Q., A. J. Waeber, and A. F. Fanning (1997), Paleoclimatic response of the closing of the Isthmus of Panama in a coupled ocean-atmosphere model, *Geophys. Res. Lett.*, 24, 253–256.
- Nisancioglu, K. H., M. E. Raymo, and P. H. Stone (2003), Reorganization of Miocene deep water circulation in response to the shoaling of the Central American Seaway, *Paleoceanography*, 18(1), 1006, doi:10.1029/2002PA000767.
- Ocean Drilling Program (2001), Shipboard Scientific Party, Leg 189 Summary, *Proc. Ocean Drill. Program Initial Rep.*, 189, 1–98.
- Omta, A. W., and H. A. Dijkstra (2003), A physical mechanism for the Atlantic-Pacific flow reversal in the early Miocene, *Global Planet. Change*, 36, 265–276.
- Otto-Bliesner, B. L., E. C. Brady, and C. Shields (2002), Late Cretaceous ocean: Coupled simulations with the National Center for Atmospheric Research Climate System Model, *J. Geophys. Res.*, 107(D2), 4019, doi:10.1029/2001JD000821.
- Paul, H. A., J. C. Zachos, B. P. Flower, and A. Tripathi (2000), Orbitally induced climate and geochemical variability across the Oligocene/Miocene boundary, *Paleoceanography*, 15, 471–485.
- Prange, M., and M. Schulz (2004), A coastal upwelling seesaw in the Atlantic Ocean as a result of the closure of the Central American Seaway, *Geophys. Res. Lett.*, 31, L17207, doi:10.1029/2004GL020073.
- Ricou, L. E. (1987), The Tethyan oceanic gates: A tectonic approach to major sedimentary changes within the Tethys, *Geodyn. Acta*, 1, 225–232.
- Royer, D. L., R. A. Berner, and D. A. Beerling (2001), Phanerozoic atmospheric CO₂ change: Evaluating geochemical and paleobiological approaches, *Earth Sci. Rev.*, 54, 349–392.
- Selten, F., M. Kliphuis, and H. A. Dijkstra (2003), Transient coupled ensemble climate simulations to study changes in the probability of extreme events, *CLIVAR Exchanges*, 8, 11–13.
- Stouffer, R. J., and S. Manabe (2003), Equilibrium response of thermohaline circulation to large changes in atmospheric CO₂ concentration, *Clim. Dyn.*, 20, 759–773.
- Trenberth, K. E., and J. M. Caron (2001), Estimates of meridional atmosphere and ocean heat transports, *J. Clim.*, 14, 3433–3443.
- van de Flierdt, T., M. Frank, A. N. Halliday, J. R. Hein, B. Hattendorf, D. Günther, and P. W. Kubik (2004), Deep and bottom water export from the Southern Ocean to the Pacific over the past 38 million years, *Paleoceanography*, 19, PA1020, doi:10.1029/2003PA000923.
- von der Heydt, A., and H. A. Dijkstra (2005), Flow reorganizations in the Panama Seaway: A cause for the demise of Miocene corals?, *Geophys. Res. Lett.*, 32, L02609, doi:10.1029/2004GL020990.
- Wade, B. S., and H. Pälike (2004), Oligocene climate dynamics, *Paleoceanography*, 19, PA4019, doi:10.1029/2004PA001042.
- Weatherly, J. W., B. P. Briegleb, W. G. Large, and J. A. Maslanik (1998), Sea ice and polar climate in the NCAR CSM, *J. Clim.*, 11, 1472–1486.
- Wright, J. D., K. G. Miller, and R. G. Fairbanks (1992), Early and middle Miocene stable isotopes: Implications for deep water circulation and climate, *Paleoceanography*, 7, 357–389.
- Zachos, J. C., M. Pagani, L. Sloan, E. Thomas, and K. Billups (2001), Trends, rhythms, and aberrations in global climate 65 Ma to present, *Science*, 292, 686–693.

H. A. Dijkstra, Department of Atmospheric Science, Colorado State University, Fort Collins CO, 80523-1371, USA.

A. von der Heydt, Institute for Marine and Atmospheric Research, Department of Physics and Astronomy, Utrecht University, Princetonplein 5, 3584 CC Utrecht, Netherlands. (a.s.vonderheydt@phys.uu.nl)